Carbohydrate Polymers 202 (2018) 600–610

Contents lists available at ScienceDirect

Carbohydrate Polymers

journal homepage: www.elsevier.com/locate/carbpol

Bioperformance of chitosan/fluoride-doped diopside nanocomposite coatings deposited on medical stainless steel

S. Karimi[a], E. Salahinejad[a,*], E. Sharifi[b], A. Nourian[c], L. Tayebi[d]

[a] Faculty of Materials Science and Engineering, K. N. Toosi University of Technology, Tehran, Iran
[b] Department of Tissue Engineering and Biomaterials, School of Science and Advanced Technologies In Medicine, Hamadan University of Medical Sciences, Hamadan, Iran
[c] Cellular and Molecular Research Center, Basic Health Sciences Institute, Shahrekord University of Medical Sciences, Shahrekord, Iran
[d] Department of Developmental Sciences, Marquette University School of Dentistry, Milwaukee, WI 53233, USA

ARTICLE INFO

Keywords:
Nanocomposite coatings
Chitosan
Fluoride-doped diopside
Bioactivity
Corrosion
Biocompatibility

ABSTRACT

This work focuses on the structure, bioactivity, corrosion, and biocompatibility characteristics of chitosan-matrix composites reinforced with various amounts of fluoride-doped diopside nanoparticles (at 20, 40, 60, and 80 wt %) deposited on stainless steel 316 L. Bioactivity studies reveal that the presence of the nanoparticles in the coatings induces apatite-forming ability to the surfaces. Based on electrochemical impedance spectroscopy and polarization experiments, the *in vitro* corrosion resistance of the substrate was enhanced by increasing the level of the nanoparticles in the coating. The sample containing 60% of the nanoparticles presented the highest osteoblast-like MG63 cell viability, in comparison to the other prepared and even control samples. Also, the cell attachment on the surfaces was improved with increasing the amount of the nanoparticles in the coatings. It is eventually concluded that the application of chitosan/fluoride-doped diopside nanocomposite coatings improves the bioperformance of metallic implants.

1. Introduction

Metallic biomaterials, particularly stainless steel 316 L, are conventionally used to fabricate certain bone fixation devices and hard tissue implants, mainly due to their suitable mechanical properties. Despite the fact that the biocompatibility of metallic biomaterials is acceptable in most cases, they disadvantageously have a low ability to bond with adjacent bone tissues. This can lead to the failure of implantation under loading, via inducing the implant lessening, mechanical damages to adjacent tissues, and pain in the patient (Bronzino & Park, 2002). Applying bioactive coatings on metallic implants can be regarded as an effective approach to overcome this drawback. From the biological perspective, a combination of bioceramics and biopolymers is a promising strategy to do so, since natural bones are mostly composed of ceramic (apatite) and polymer (collagen) components. From the viewpoint of the materials science, certain substances cannot alone provide the desirable mechanical and chemical properties required for a particular purpose, which can be addressed by employing composites comprising of multiple substances.

Chitosan is a natural biopolymer used in medical applications due to its excellent biocompatibility, biodegradability, antibacterial activity and accelerating character in wound healing and injury. However, this polymer suffers from poor mechanical properties and a low ability to encourage the bone formation (Chandy & Sharma, 1990; Di Martino, Sittinger, & Risbud, 2005; Khor & Lim, 2003). Ceramics have attracted a lot of attention in this field because they bond well to bones and cause little adverse reactions with the body. As well as widespread studies conducted on chitosan-matrix composites reinforced with apatites (Abe, Kokubo, & Yamamuro, 1990; Kong et al., 2006; Li et al., 2005; Lin & Yeh, 2004; Tanahashi et al., 1994), bioglasses (Luz & Mano, 2012; Mota et al., 2012), and glass ceramics (Peter, Binulal, Nair et al., 2010; Peter, Binulal, Soumya et al., 2010; Kumar et al., 2014) showed that the addition of diopside ($MgCaSi_2O_6$) to chitosan-based scaffolds improves the bioactivity, protein adsorption, and biocompatibility of the products. Diopside belongs to the category of magnesium-containing silicates, which are suitable candidates for the replacement and regeneration of hard tissues due to suitable mechanical behavior, biocompatibility, and bioactivity (Diba, Goudouri, Tapia, & Boccaccini, 2014; Diba, Tapia, Boccaccini, & Strobel, 2012). In this regard, it is known that the incorporation of fluoride into diopside at a certain content induces a better bioactivity and biodegradability to this bioceramic (Baghjeghaz & Salahinejad, 2017; Salahinejad & Baghjeghaz, 2017). In this research, for the first time, chitosan/fluoride-doped diopside nanocomposite coatings were coated on medical-grade stainless steel 316 L. The

* Corresponding author.
E-mail address: salahinejad@kntu.ac.ir (E. Salahinejad).

https://doi.org/10.1016/j.carbpol.2018.09.022
Received 10 May 2018; Received in revised form 12 September 2018; Accepted 13 September 2018
Available online 14 September 2018
0144-8617/

selection of this polysaccharide as the coating matrix is based on the criterion that the biocompatible, biodegradable and hydrophilic characters of chitosan help to mimic the polymeric constitute of natural bone. The hypothesis is that by incorporating fluoride-doped diopside (FD) nanoparticles into chitosan-based coatings, the apatite-formation ability, corrosion protection, and biocompatibility of the coatings are altered. Thus, the bioperformance of the specimens was *in vitro* studied as a function of the relative percentages of the constitutes of the composite coatings.

2. Materials and method

2.1. Materials used

In order to synthesize FD, silicon tetrachloride ($SiCl_4$, Merck, Germany, > 99%), calcium chloride ($CaCl_2$, Merck, Germany, > 98%), magnesium chloride ($MgCl_2$, Merck, Germany, > 98%) and magnesium fluoride (MgF_2, Alfa Aesar, USA, > 98%) were used as precursors. Also, pure ethanol (C_2H_5OH, Merck, Germany, > 99.9%) and ammonia solution (NH_4OH, Merck, Germany, 25%) were used as the solvent and precipitant, respectively. Chitosan (Deacetylated Chitin, Poly D-glucosamin, Sigma Aldrich-448877) with the mean deacetylation degree of 84.2% and the molecular weight of 140,469.4 $g.mol^{-1}$ (Garcia et al., 2018) was also employed as the polymeric constitute of the composite coatings. In addition, acetic acid ($C_2H_4O_2$, Mojallali, Iran, > 99.9%), distilled water and pure ethanol were utilized to prepare nanocomposite sols. Medical-grade stainless steel 316 l (Goodfellow Cambridge Ltd, UK) was also used as the substrate.

2.2. Sample preparation

FD powders containing 1 mol% fluoride were synthesized by a co-precipitation method according to Refs. (Baghjeghaz & Salahinejad, 2017; Esmati, Khodaei, Salahinejad, & Sharifi, 2018; Salahinejad & Baghjeghaz, 2017). In brief, $CaCl_2$, $MgCl_2$, $SiCl_4$, and MgF_2 at the molar ratio of 1:0.95:2:0.05 were added to ethanol in an ice-water bath. After complete dissolution, the ammonia solution was added under stirring until pH of 10. The obtained precipitates were then dried at 100 °C and followed by calcination at 700 °C for 2 h. It is worth noting that based on Refs. (Baghjeghaz & Salahinejad, 2017; Salahinejad & Baghjeghaz, 2017), this level of fluoride doped in diopside was the optimal incorporation to meet the highest bioactivity. In order to prepare nanocomposite sols, 0.1 g chitosan was first dissolved in 2 ml of acetic acid, 78 ml of distilled water and 20 ml of ethanol. Then, 0.025, 0.067, 0.15 and 0.4 g of the calcined FD powder were added to the above solution and sonicated for 1 and 2 h to make composites containing 20, 40, 60 and 80 wt% of FD, respectively. Medical-grade stainless steel 316 l substrates were prepared by polishing to #2000 and washing with acetone, ethanol and water under ultrasonication.

The treated substrates were dipped into the prepared sols at the immersion and withdrawal speeds of 30 mm/s. Then, the samples were kept at room temperature for 24 h. In order to increase the thickness and efficiency of coating, the second and third layers of the sols were coated on the samples with the same method. Hereafter, the uncoated substrate will be referred to as S-Uncoated, and the coated samples containing 20, 40, 60 and 80% of the nanoparticles are coded as S-20%, S-40%, S-60%, and S-80%, respectively.

2.3. Structural characterization of the coated samples

X-ray diffraction (XRD, PANalytical, X'pert Pro MPD, Cu-Kα radiation, step size: 0.03°, step time: 3 s, 2θ range: 10-80°), Fourier transform infrared spectrometry (FTIR, Avaspec 2048 TEC Avantes, KBr pellet technique, resolution: 4 cm^{-1}, wavenumber range: 400-2000 cm^{-1}), and field emission scanning electron microscopy (FESEM, MIRA3TESCAN-XMU, accelerating voltage: 15 kV) were used to characterize the calcined FD powder. The mean size of the synthesized particle particles was estimated by image-analyzing of the taken micrographs. FESEM was also utilized to study the morphology of the coatings.

2.4. Bioactivity assessment

The samples were immersed in the simulated body fluid (SBF) prepared according to Ref. (Kokubo & Takadama, 2006) at 36 ± 0.5 °C for 14 days in an incubator. The samples were then washed out and dried at room temperature. In order to investigate the morphology of the specimens after immersion in the SBF, FESEM equipped with energy-dispersive X-ray spectroscopy (EDS) was used.

2.5. Electrochemical studies

The corrosion behavior of the samples was investigated in the SBF at 37 °C using a potentiostat device (Vertex, Ivium Technologies). A standard platinum wire and standard Ag/AgCl electrode were used as auxiliary and reference electrodes, respectively. The samples were first kept in the solution for 2 h to achieve open circuit potential (OCP). Electrochemical impedance spectroscopy (EIS) was conducted over the frequency ranges of 5 kHz to 10 mHz with the potential amplitude of 10 mV at the OCP. Afterwards, potentiodynamic polarization experiments in the same solution were conducted at a scanning rate of 1 mV/s in the potential range of -0.6 V to +1 V.

2.6. Biocompatibility evaluations

Prior to studying cell responses, the samples were first immersed in a 70% ethanol solution for 2 h and washed several times with phosphate-buffered saline (PBS). The sterilization process was completed by placing the disks under UV for 20 min. $2*10^4$ osteoblast-like MG63 cells were cultured on the sterilized discs for 24 and 48 h in the humidified medium containing 5% CO_2 at 37 °C. The evaluation of cell viability was performed using the MTT assay with three repetitions, according to Refs. (Sharifi, Azami et al., 2016; Sharifi, Ebrahimi-Barough et al., 2016). The optical density (OD) of viable cells on each well was measured by a UV spectrophotometer (Elisa Reader, Awareness, Stat Fax3200, USA). Also, the analysis of variance (ANOVA) approach was conducted on the results, with the significance level of $p < 0.05$.

Also, in order to analyze the morphology of osteoblast-like MG63 cells cultured for 24 and 48 h after cell fixation, the specimen surfaces were observed by a scanning electron microscope (SEM, Hitachi, SU3500).

3. Results and discussion

3.1. Characterization of the synthesized particulate reinforcement

The XRD pattern of the FD powder synthesized by the coprecipitation and subsequent calcination processes is shown in Fig. 1(a). According to the analysis performed by the PANalytical X'pert highscore software, the FD powder has a single-phase diopside structure ($MgCaSi_2O_6$, Ref. Code: 00-017–0318) without any secondary phases. Using the Scherrer equation, the mean size of diopside crystallites is determined to be 52 nm, based on the strongest peak ($2\ \bar{2}\ 1$) at $2\theta = 34.7°$. The FTIR spectrum of the FD powder is also depicted in Fig. 1(b). As well as the absorption bands of diopside (O-Ca-O at 400 cm^{-1}, O-Mg-O at 465 and 525 cm^{-1}, O-Si-O at 635 and 672 cm^{-1}, and Si-O at 860, 960, 1070 cm^{-1}), which is compatible with Refs. (Baghjeghaz & Salahinejad, 2017; Salahinejad & Baghjeghaz, 2017; Salahinejad & Vahedifard, 2017), two peaks at the wavenumbers of 804 and 930 cm^{-1} correspond to the tensile mode of the Si-F bond, indicating the introduction of fluoride into diopside. Fig. 1(c) indicates the FESEM image of a batch of the FD powder. As seen, the particles are angular-

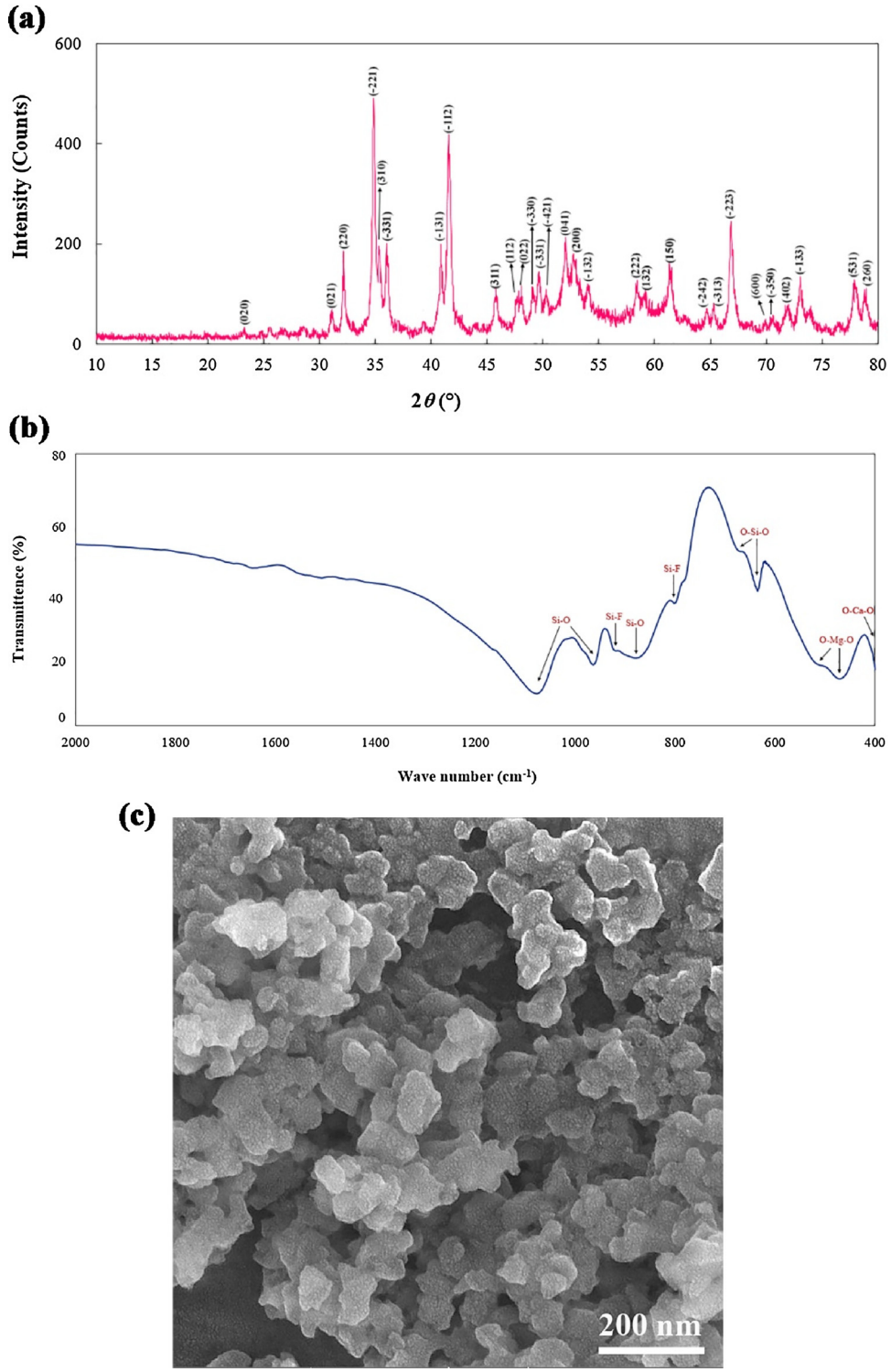

Fig. 1. XRD pattern (a), FTIR spectrum (b) and FESEM micrograph (c) of the FD powder used as the coating reinforcement.

shaped with an average diameter of 60 nm.

3.2. Characterization of the deposited coatings

The FESEM micrograph of the samples is demonstrated in Fig. 2. As can be seen in Fig. 2(b)–(e), the coatings deposited after 2 h of the sol sonication have desirable features with a uniform and crack-free character. On the contrary, the sonication of the sol for 1 h had led to the creation of cracks in the vicinity of some reinforcing particles for S-80% (Fig. 2(f)). Thus, the samples prepared by the sol sonication of 2 h were used for the following studies.

3.3. Apatite-forming ability

In order to evaluate the *in vitro* bioactivity of the samples, the uncoated (control) and coated discs were soaked in the SBF for 14 days. According to Fig. 3(a), the stainless steel substrate exhibits no remarkable apatite-formation ability. However, the FESEM micrograph of

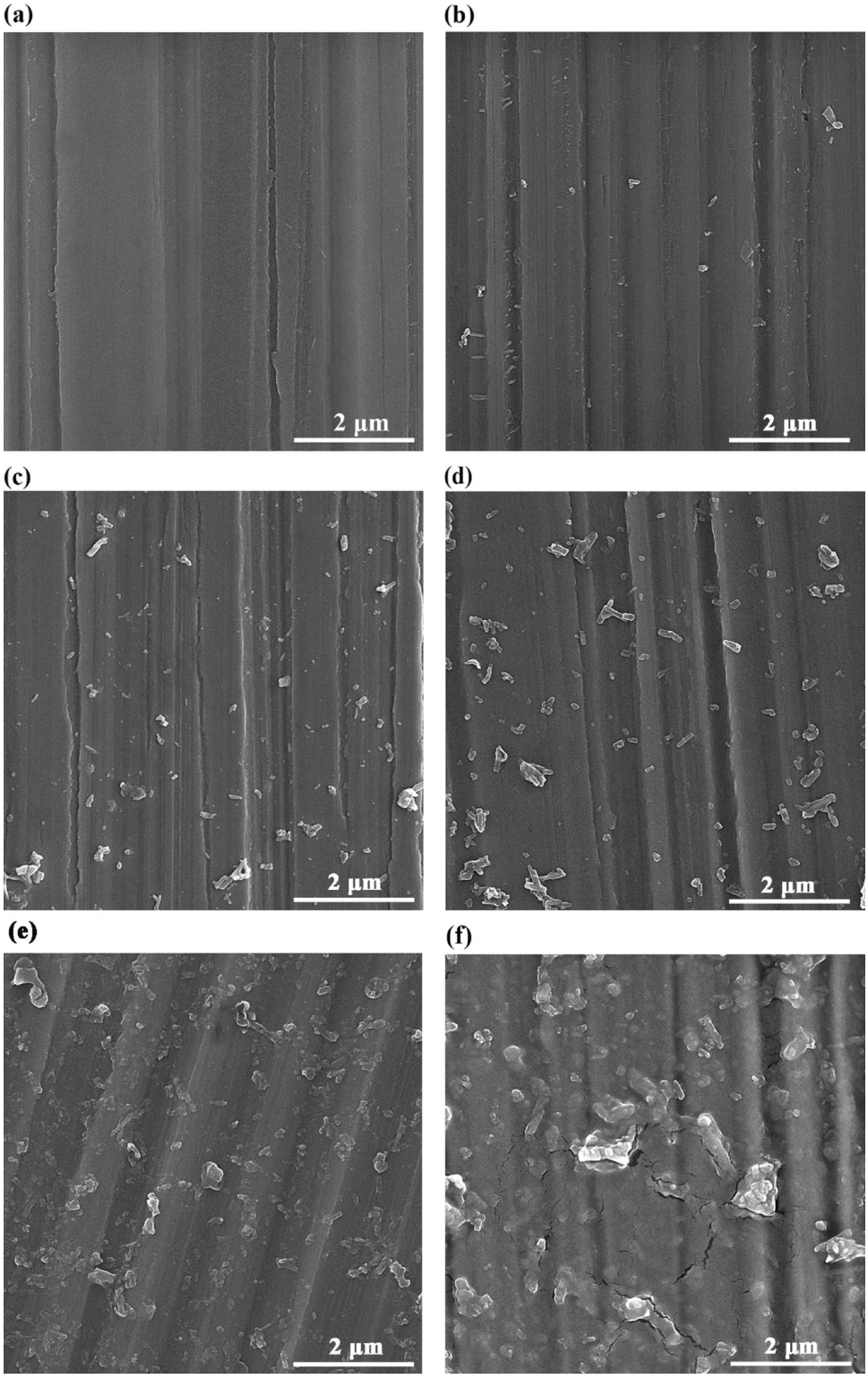

Fig. 2. FESEM micrographs of the uncoated substrate (a) and the coated samples with the sol sonication for 2 h: S-20% (b), S-40% (c), S-60%, (d), S-80% (e), and S-80% with the sol sonication for 1 h (f).

the soaked S-20% sample (Fig. 3(b) and (c)) indicates the formation of precipitates, especially around the reinforced particles. To determine the chemical composition of the precipitates formed after immersion in the SBF, the EDS analysis was conducted on the precipitates (Fig. 3(d)). The presence of phosphorus in the pattern suggests the formation of apatite, whereas calcium detected can be related to both the coating particles and apatite precipitates. Iron, chromium and nickel elements are also signals from the 316 l stainless steel substrate, while oxygen, carbon, fluoride, silicon and magnesium detected are related to the chitosan and FD phases.

Comparing the apatite-formation ability of the control and coated samples, it is accordingly concluded that the application of the nano-composite coatings induces bioactivity to stainless steel. On the one hand, the cationic and hydrophilic natures of chitosan encourage the

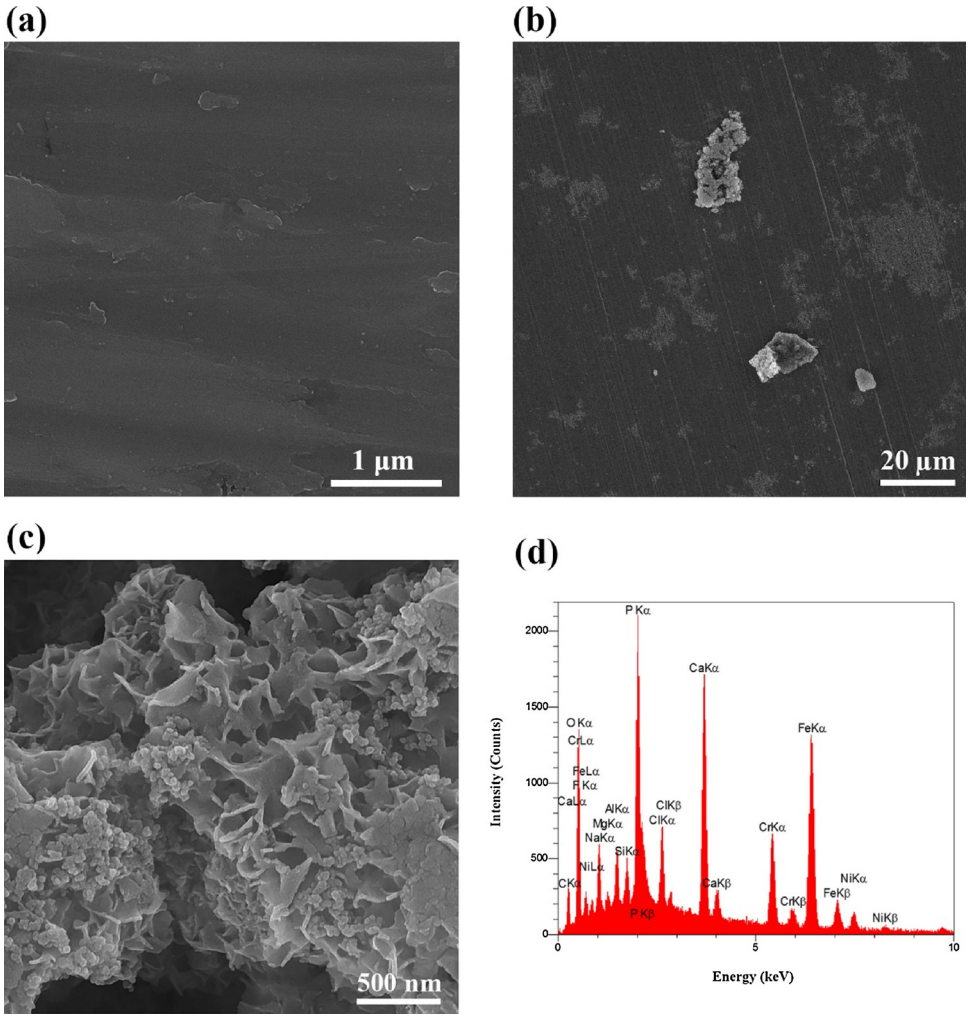

Fig. 3. FESEM images of the uncoated sample (a) and S-20% sample in two magnifications (b, c) and EDS pattern taken of the S-20% sample (d) after 14 days of soaking in the SBF.

adsorption of phosphate ions and thereby the apatite precipiattain (Baskar, Balu, & Kumar, 2011; Tanahashi & Matsuda, 1997). On the other hand, diopside is essentially bioactive via some ion-exchnage reactions (Cai et al., 2009; Martens & Harriss, 1970; Salahinejad & Vahedifard, 2017; Vahedifard & Salahinejad, 2017). The presense of fluoride in diopside also increases the stability of precipitated apatite against dissolution in the SBF (Baghjeghaz & Salahinejad, 2017; Salahinejad & Baghjeghaz, 2017).

3.4. Corrosion behavior of the samples

The corrosion behavior of the samples was investigated in the SBF at 37 °C by the EIS and polarization experiments. Fig. 4 presents the EIS Nyquist and Bode impedance plots of the samples. The Nyquist diagrams of all the samples indicate arches of scattered circles, representing a non-ideal capacitance behavior due to the heterogeneity and roughness of the electrode surfaces. To apply these contributions, constant phase elements instead of ideal capacitors are used in the following equivalent circuit modelling of the EIS data. It is observed that by applying the coatings (via the comparison of the coated sample with the uncoated samples) and by increasing the amount of the nanoparticles in the coatings, the diameter of the arc of the circles increases in the Nyquist diagrams, as indicative of the increase in the corrosion resistance. Also, EIS Bod-impedance and Bod-phase plots indicate a shoulder and a peak, respectively, representing a capacitive relaxation time in the corresponding equivalent circuit. It is evident in the Bod plots that by applying the coatings and increasing the amount of the nanoparticles, the impedance values increase and the capacitor region is transferred to lower frequencies. In addition, the failure frequency (frequency at 45 degrees) decreases by applying the coatings and by increasing the amount of the nanoparticles. Therefore, it is discovered that by increasing the amount of the nanoparticles, the separation zone is reduced and the performance of the coatings as a barrier against corrosion attack is improved. That is, the corrosion resistance of the substrate is increased by using the coatings and by increasing the amount of the nanoparticles in the coatings.

Based on the feature of the EIS plots, a circuit according to Fig. 5 was used to model the EIS experimental data by using the Ivioum software. In this circuit, in addition to the electrolyte resistance (R_s), a constant phase element (CPE_{dl}) of the double layer parallel to a charge transfer resistance (R_{ct}) associated with the polarization resistance at the solution-electrode interface was considered. The impedance (Z_{CPE}) of a CPE is expressed as (E Salahinejad et al.):

$$Z_{CPE} = \frac{1}{Y_0(j\omega)^{-n}} \quad (1)$$

where Y_0 is the capacitance in F, ω is the angular frequency ($\omega = 2\pi f$; f is the frequency in Hz), j is $(-1)^{0.5}$, and n is an empirical exponent that is less than one and describes the deviation of the real system from an ideal capacitor. The parameters obtained from the fitting of the experimental EIS data with the proposed equivalent circuit are tabulated in Table 1. In addition, the experimental EIS data and modeled curve

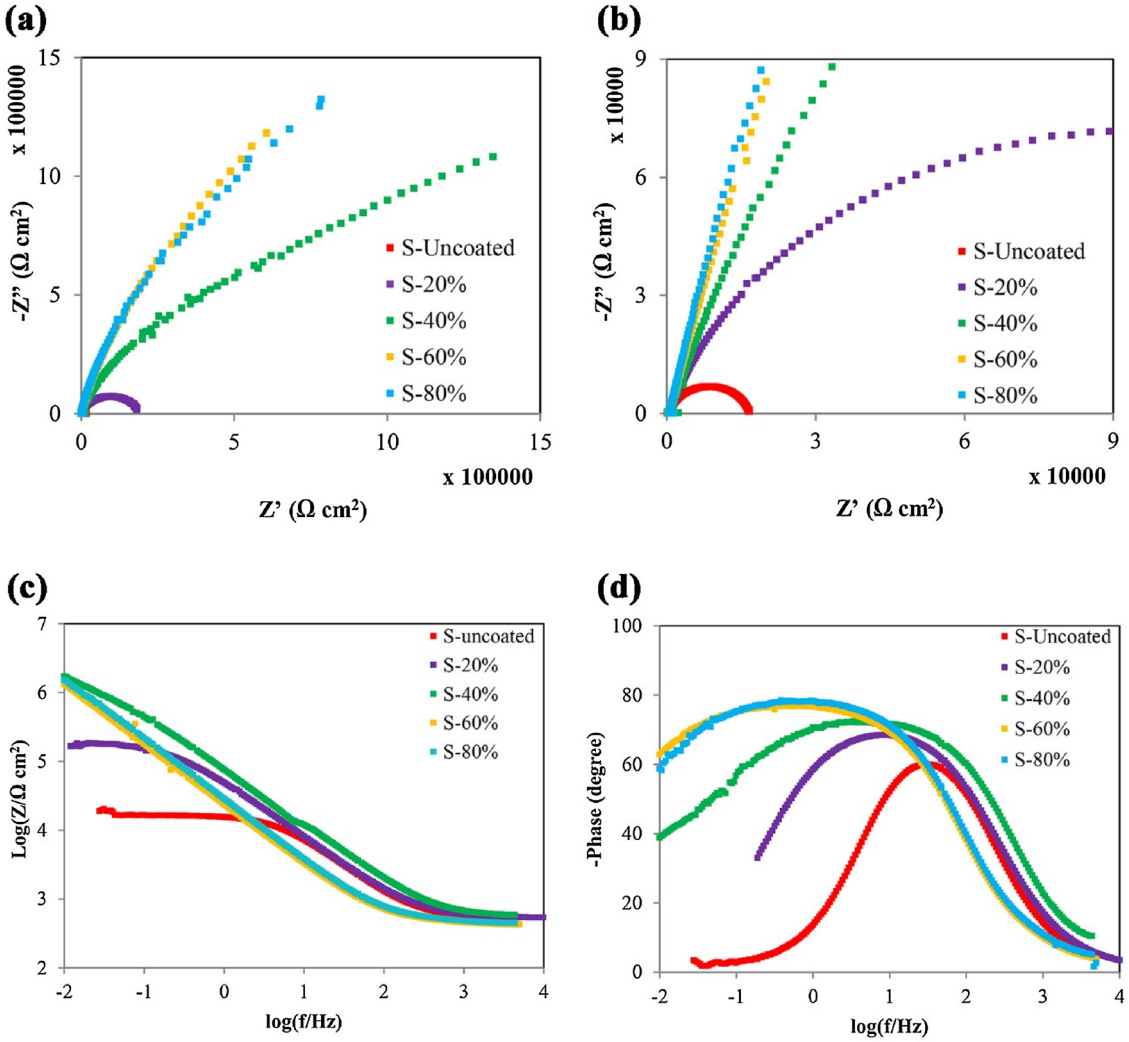

Fig. 4. EIS results of the samples: Nyquist (a), magnified Nyquist (b), Bode-impedance (c), and Bode-phase angle (d) plots.

for the substrate are, for example, presented in Fig. 5, which indicates an appropriate adaptation and the merit of the modeling.

In addition, the equivalent capacitance of the double layer (C_{dl}) and the corrosion protection efficiency of the coatings based on the impedance analysis (η_I) relative to the charge transfer resistance of the substrate (R°_{ct}) were calculated by Eqs. (2) and (3), respectively (Ehsani, Moshrefi, & Ahmadi, 2015; Yadav, Kumar, Kumari, Bahadur, & Ebenso, 2015) and listed in Table 1.

$$C_{dl} = (Y_0 \bullet R_{ct}^{1-n})^{\frac{1}{n}} \tag{2}$$

$$\eta_I = (1-\frac{R_{ct}^0}{R_{ct}}) \times 100 \tag{3}$$

In accordance to Table 1, by increasing the amount of the nanoparticles in the coatings, C_{dl} is decreased and η_I is enhanced. Based on Eq. (4), the reduction in the capacity suggests an increase in the double layer thickness and/or the decrease in the coating dielectric constant affected by the porosity, wettability and composition of the coatings.

$$C_{dl} = \frac{A\varepsilon\varepsilon_0}{d} \tag{4}$$

where ε_0 and ε are the dielectric constant of the vacuum and environment, A is the exposed area and d is the thickness of the double layer (Liu et al., 2007; Salahinejad et al., 2013). The dielectric constant is a physical characteristic that is determined by atomic/molecular interactions and is proportional to the solvent ability to separate ions from the sample toward the electrolyte. In general, materials with high dielectric constants, when subjected to intensive electrical fields, are more easily deteriorated compared with those with low dielectric constants (Jouyban, Soltanpour, & Chan, 2004). This is in agreement with the results of this study, due to the realized increase in the corrosion resistance by decreasing the capacity. In addition, the increase in the protection efficiency (= the increase in the corrosion resistance) with the amount of the nanoparticles confirms the qualitative conclusions drawn from Fig. 4. As can be seen, the maximum protection efficiency belongs to S-80%, which is 99.99%. Albeit the proximity of this parameter to 100% does not mean that this sample is corroded at all. Instead, according to Eq. (3) and Table 1, this is due to the fact that the charge transfer resistance on this surface is much larger than that on the uncoated sample.

The polarization curves of the samples in the SBF are shown in Fig. 6. Related corrosion parameters, including corrosion potential (E_{corr}), corrosion current density (i_{corr}), β_a and β_c (anodic and cathodic Tafel slopes, respectively) were extracted from the extrapolation of the Tafel curves using the Ivium software (Table 1). In addition, the polarization resistance (R_p) by the Stern-Geary equation (Eq. (5)) (Bakhsheshi-Rad et al., 2016), the corrosion rate (CR) (Eq. (6)), and the protection efficiency (η_p) of the coatings based on the polarization analysis (Eq. (7)) (Groysman, 2009) were also determined and listed in Table 1.

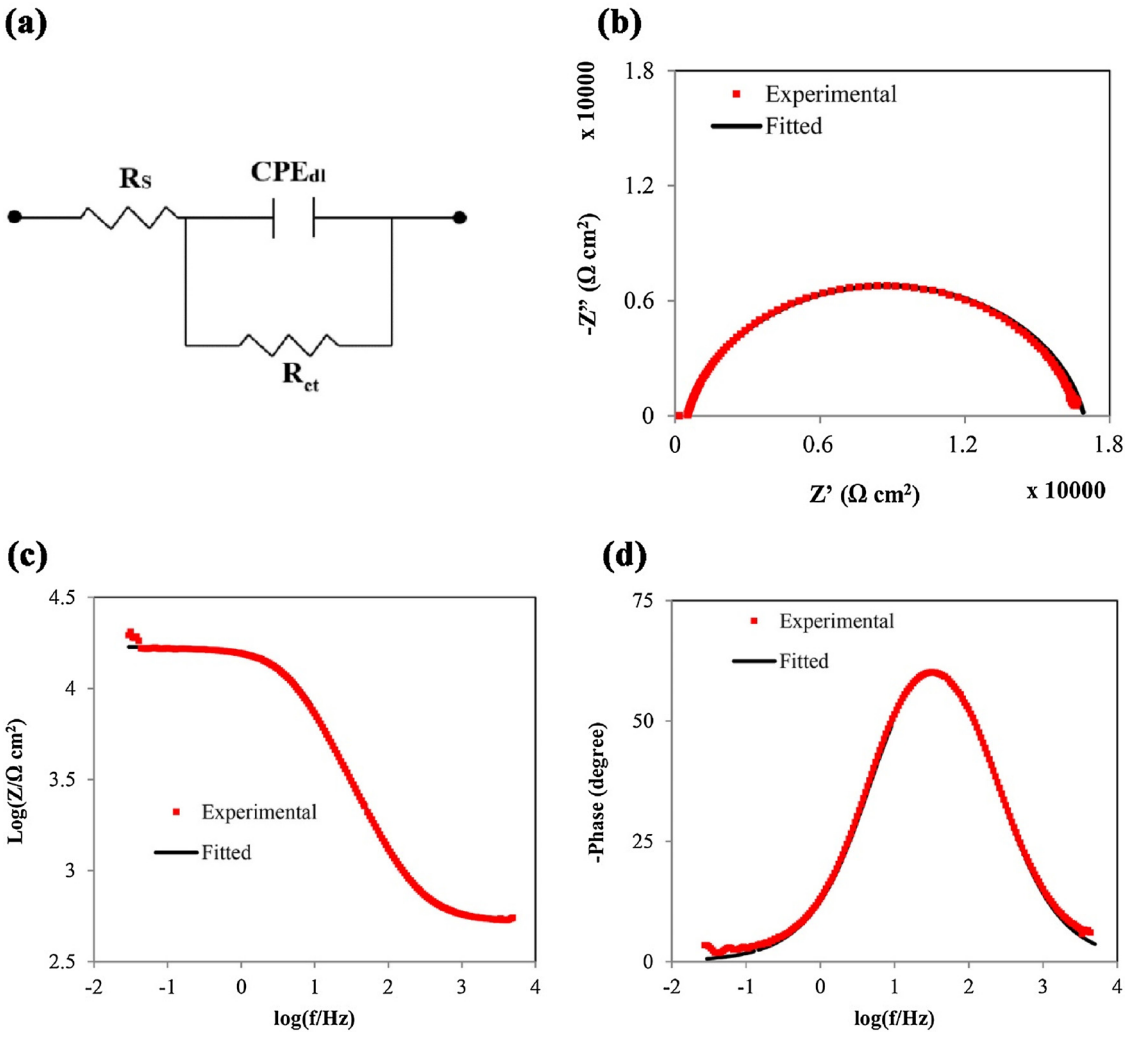

Fig. 5. Equivalent electrical circuit used for the modelling of the EIS spectra (a) and the comparison of the experimental and fitted data: Nyquist (b), Bode-impedance (b), and bode-phase angle (c) representations.

$$R_p = \frac{\beta_a \beta_c}{[2.3 \times i_{corr}(\beta_a + \beta_c)]} \quad (5)$$

$$CR = K\frac{i_{corr}}{\rho}EW \quad (6)$$

$$\eta_P = (1-\frac{i_{cor}}{i^0_{cor}}) \times 100 \quad (7)$$

where K is a constant and equals to 8.954×10^{-3} mmg/μA.cm.yr, ρ is the substrate density in g/cm^3, EW is the equivalent weight in g, and i°_{cor} is the current density of the uncoated sample in μA/cm^2.

Corrosion potential is a measure of tendency to corrosion, where a more positive potential indicates a lesser tendency to corrosion in that environment. In accordance with Fig. 6 and Table 1, the corrosion potential in the coated samples increases with increasing the percentage of the nanoparticles. This indicates that the coatings with the higher percentages of the nanoparticles are less porous (more dense) and more effectively prevents the SBF from reaching the metal substrate. On the other hand, the corrosion potential of the uncoated sample is higher than the other samples and close to S-80%. In this regard, it should be noted that the corrosion potential depends on relative responses between the cathode and anode during the polarization test and is not always related to the corrosion resistance, especially when the surface conditions of the samples are completely different, such as the samples of this study which are in two different categories: without coatings and with insulating coatings. Therefore, in order to better compare the corrosion resistance of the samples, it is better to refer to the other parameters, like the corrosion current density, corrosion rate and

Table 1
EIS parameters derived from the equivalent electrical circuit modelling and the polarization curves.

Sample	R_s (Ω cm^2)	R_{ct} (Ω cm^2)	Y_0 (μΩ^{-1} cm^{-2})	n	C_{dl} (μF cm^{-2})	η_I (%)	E_{corr} (V)	I_{corr} (μA/cm^2)	β_a (V/dec)	β_c (V/dce)	R_p (ohm)	CR (mm/year)	η_P (%)
S-Uncoated	535	1.68×10^4	1.91	0.863	9.92	–	−0.129	14.12	0.158	0.145	1.861×10^4	0.1431	–
S-20%	534	1.92×10^5	1.30	0.872	8.27	91.25	−0.371	3.04	0.352	0.093	8.394×10^4	0.0308	78.47
S-40%	1360	3.11×10^6	0.92	0.877	7.40	99.47	−0.198	1.50	0.201	0.143	19.37×10^4	0.0152	89.38
S-60%	430	4.12×10^6	0.82	0.895	4.78	99.59	−0.189	0.68	0.134	0.122	32.74×10^4	0.0069	95.18
S-80%	449	4.46×10^6	0.55	0.897	1.11	99.99	−0.100	0.25	0.141	0.122	90.54×10^4	0.0025	98.23

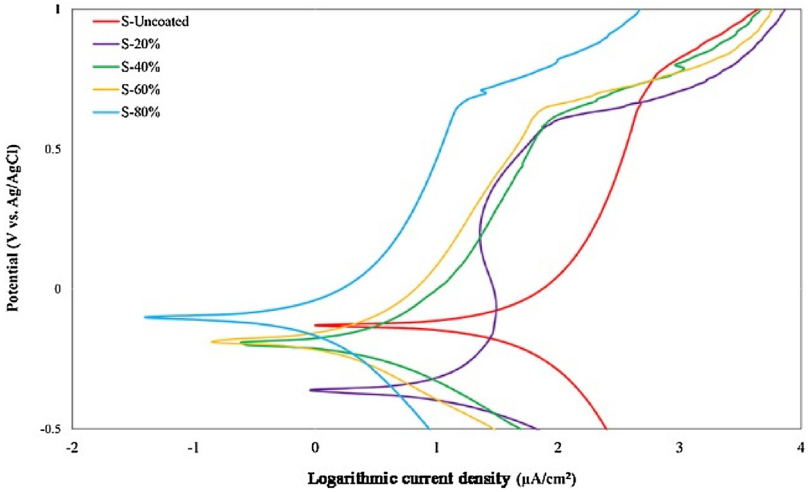

Fig. 6. Potentiodynamic polarization curves of the samples.

polarization resistance.

According to Table 1, the corrosion current density and corrosion rate for the coated samples were less than those for the uncoated sample, where these parameters were decreased by increasing the percentage of the nanoparticles in the coatings. Also, by using the coatings and by increasing the percentage of the nanoparticles, the polarization resistance and protection efficiency were significantly increased. Therefore, it is concluded that the corrosion resistance in the SBF was enhanced by increasing the amount of the nanoparticles, which is in agreement with the results of EIS. The use of the coatings, on the one hand, leads to the creation of a physical insulating barrier between the substrate and corrosive environment. On the other hand, the lower degradation rate of the ceramic nanoparticles compared to chitosan is the reason of the improvement in the corrosion resistance by increasing the percentage of the nanoparticles. Similarly, in a study (Hahn et al., 2011) that investigated the corrosion behavior of chitosan-hydroxyapatite composite coatings (with the different percentages of chitosan: 5, 10 and 20 wt%) deposited on magnesium, an increase in the amount of chitosan increases the corrosion current density and, consequently, increases the corrosion rate, which is attributed to the lower resistance of chitosan compared to hydroxyapatite against *in vitro* degradation.

3.5. Cell viability and attachment

The MTT assay was performed on the MG63 cell cultures conducted on the specimens. As shown in Fig. 7, the level of cell compatibility for all the samples at 24 h of culture is near to that of the control ($p > 0.05$). The increase in the OD of viable cells from 24 h to 48 h for all the samples ($p < 0.05$) suggests cell proliferation, where the proliferation rates of S-uncoated, S-20%, S-40%, S-60%, and S-80% were 63, 109, 116, 136 and 90%, respectively. Typically, at 48 h of culture, the cell cytocompatibility of all the coated samples becomes greater than the uncoated sample, especially for S-40%, S-60%, and S-80% based on the ANOVA analysis. In this regard, the best behavior was found for the S-60% sample, so that its cell viability with respect to the uncoated sample reached almost 147% at 48 h.

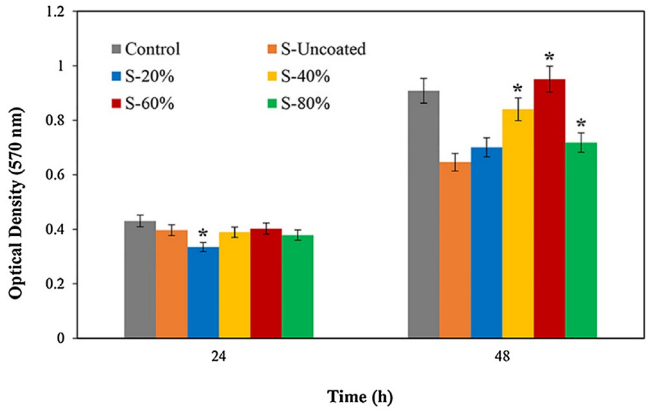

Fig. 7. MTT results in terms of OD, where * represents $p < 0.05$ with respect to the uncoated sample.

According to the MTT results, the uncoated sample exhibits a high cytocompatibility over the culture period of 24 h. However, in comparison to the other samples, a significant cell proliferation did not occur to 48 h for this sample, which is due to the release of undesired metal ions. According to the results of the corrosion tests, on the one hand, the coatings improve the corrosion resistance and reduce the release of metal ions in the environment. On the other hand, the components of the coatings play a positive role in cytocompatibility. Chitosan as a natural biopolymer has a high biocompatibility. Diopside is also effective in the proliferation and differentiation of cells via releasing silicon, magnesium and calcium ions (Razavi et al., 2014; Wu & Chang, 2007). The competition between these two components determines the cellular behavior among the coated samples. Similarly, cell viability on chitosan-hydroxyapatite, chitosan-calcium phosphate and chitosan-bioglass composites (Kim, Knowles, & Kim, 2005; Luz & Mano, 2012; Rochet et al., 2009; Teng et al., 2009; Wang et al., 2009) has increased by adding bioceramics to an optimal amount. Therefore, it is concluded that in the coatings containing 20, 40, and 60% of the FD nanoparticles, the positive effect of the release of silicon, magnesium and calcium ions from FD determines cellular behavior, so that the increase in the amount of the nanoparticles improved the viability in 48 h of culture. However, the lower viability of the S-80% sample compared to S-60% shows that in these large amounts of the nanoparticles, the reduction of the amount of chitosan (as a biopolymer with excellent biocompatibility) (Jun et al., 2010) and the extreme release of magnesium ions (Serre, Papillard, Chavassieux, Voegel, & Boivin, 1998) from the nanoparticles have been the dominant mechanism in cytocompatibility.

The SEM images of the cells cultured for 24 and 48 h on the surfaces are shown in Figs. 8 and 9, respectively. Particularly for 24 h of culture, a very low number of cells were observed only on limited zones of the uncoated sample surface. However, there were more cells on the coated samples, where some of them have a round morphology and some have a flatter morphology. This improvement in the cellular attachment is attributed to both the biocompatible components of the coatings. The

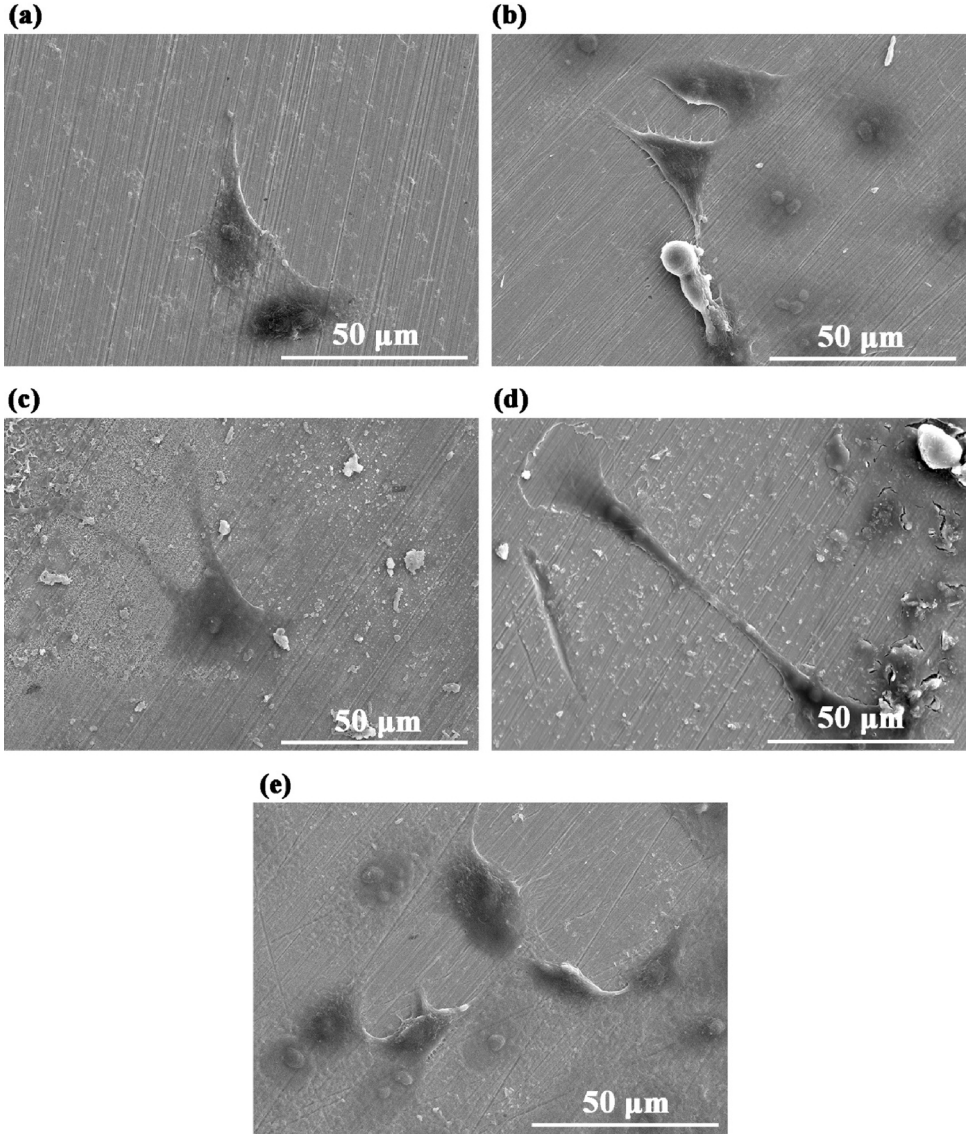

Fig. 8. SEM micrograph of cells cultured for 24 h on the samples: S-uncoated (a), S-20% (b), S-40% (c), S-60% (d), and S-80% (e).

presence of chitosan in the coatings leads to an improvement in the cell adhesion, due to the structural similarity with glycosaminoglycan which is an extracellular molecule and plays a key role in cellular morphology regulating and functions (Hahn et al., 2011; Wang, de Boer, & De Groot, 2004). Regarding the ceramic component, it is noteworthy that the morphology of well-spread cells with stretched branches is overall improved in this rank: S-20%, S-40%, S-60% and S-80%. That indicates the improvement in the cell adhesion with increasing the nanoparticles in the coatings. This behavior is consistent with some references (Singh, Singh, & Singh, 2012; Thein-Han & Misra, 2009) suggesting that cell adhesion is improved with increasing biocompatible nanoparticles in polymer-matrix composites. The increase in the amount of nanoparticles in composite coatings enhances the surface roughness and hydrophilicity, which leads to an increase in the ability of the sample surface to absorb the protein and thereby a better adhesion of the cells. These contributions can be explained as follows:

a) *Surface roughness*: According to the SEM images taken from the coating surfaces, the roughness of the coatings increases with increasing the concentration of the ceramic nanoparticle. It has been shown that by enhancing the surface roughness, cell adhesion is also improved (Teng et al., 2009), since the absorption of proteins increases (Peter, Binulal, Nair et al., 2010). In this regard, the study of MG63 cell culturing on chitosan-gelatin and chitosan-gelatin-hydroxyapatite (HA) scaffolds has shown that the cell adhesion on the HA-containing samples with higher roughness is better than the chitosan-gelatin species (Peter, Ganesh et al., 2010). A similar behavior for cell adhesion on PCL-HA scaffolds has been reported by increasing ceramic percentage and roughness (Yu, Wooley, & Yang, 2009). In this regard, the increase in wettability with roughness and thereby the improvement in cell adhesion are also noticeable.
b) *Nanometric dimensions of the ceramic particles*: The presence of the fine and nanoscale particles of NF in the coatings, via increasing the surface area, leads to an enhancement in the surface interactions with proteins, which results in better cell adhesion. In a study conducted on the behavior of MG63 cells on chitosan-gelatin-bioglass composites, the improvement of cell adhesion, apart from the surface roughness, has been attributed to the increase of the surface area in the presence of the nanoparticles, where both result in greater absorption of proteins (Peter, Binulal, Nair et al., 2010).
c) *Wettability*: The intrinsic property of surface hydrophilicity, by encouraging the formation of effective functional groups, results in more protein absorption and an improvement in cell adhesion. In a study of cell adhesion on pure chitosan, chitosan/SiCaP, and

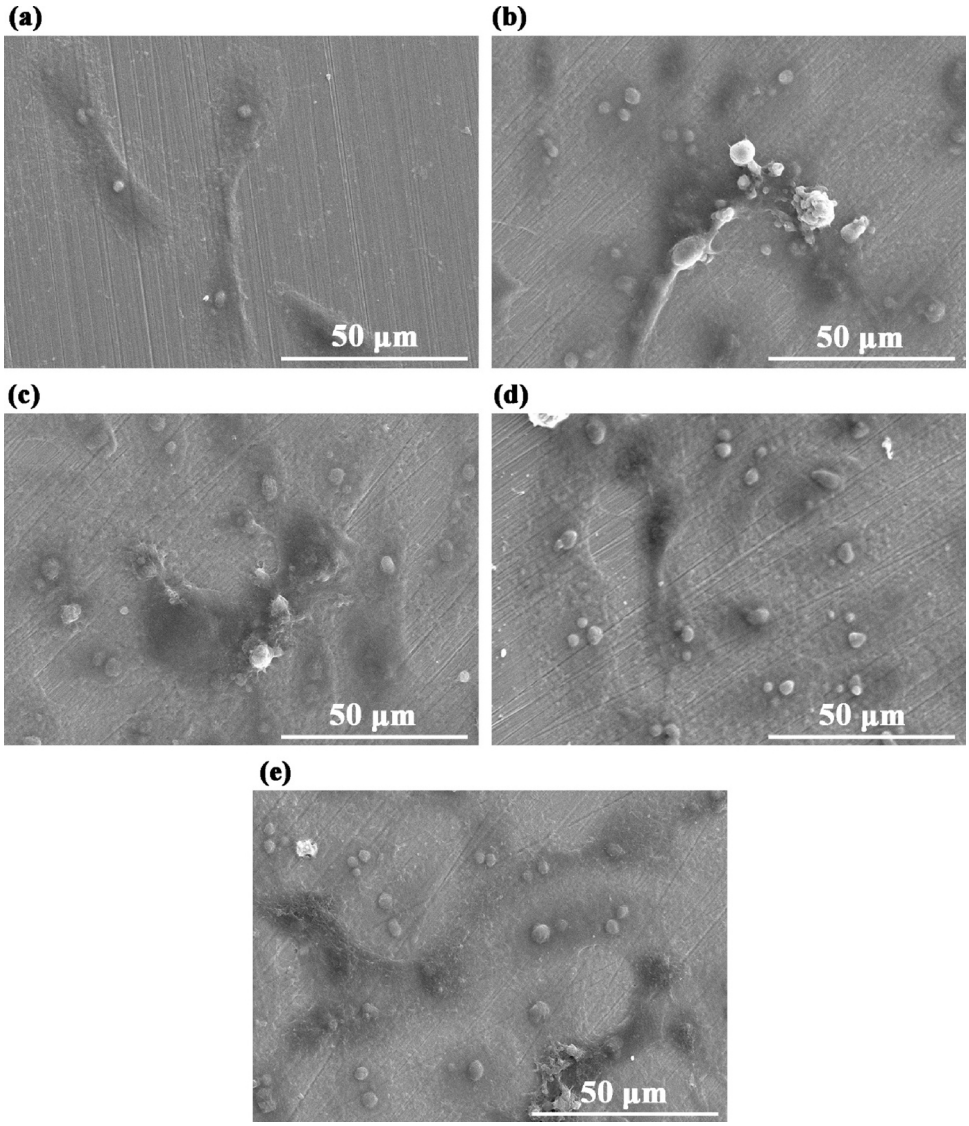

Fig. 9. SEM micrograph of cells cultured for 48 h on the samples: S-uncoated (a), S-20% (b), S-40% (c), S-60% (d), and S-80% (e).

chitosan/SiCaPMg membranes, the increase of hydrophilicity in the membrane containing SiCaPMg resulted in a higher protein absorption, whereas the surface roughness of the sample containing SiCaP was higher than the other membranes (Luz & Mano, 2012). Diopside is also a hydrophilic ceramic, as it is easily hydrolyzed in neutral solutions like other silicate ceramics. Its wettability leads to the formation of Si − OH functional groups and reacts with protein functional groups through electrostatic and van der Waals forces, improving the level of cell adhesion (Hosseini, Emadi, Kharaziha, & Doostmohammadi, 2017). In this regard, it has been shown that osteoblast cells grown on hydrophilic materials are distinct and plate-shaped plaques, whereas the cell adhesion on the surface of hydrophobic materials is much lower (Lim, Taylor, Li, Vogler, & Donahue, 2005; López-Pérez, da Silva, Serra, Pashkuleva, & Reis, 2010).

It is worth noting that despite the higher cell viability of S-60% compared with S-80% according to the MTT assay, the cell adhesion on S-80% is better. This difference arises from the fact that cell viability is mostly influenced by the release of ions from biomaterials; however, cell adhesion mostly depends on the surface properties of the biomaterial (roughness, wettability, protein adsorption, etc.). In other words, the lower cell viability of S-80% than S-60% is attributed to the extreme ionic release from its ceramic component, whereas its higher roughness and hydrophilicity explain its better cellular adhesion. For confirmation of this issue, it has been shown that the higher degradation rate of chitosan/SiCaP composite membranes than chitosan/SiCaPMg membranes has reduced its cell viability (Luz & Mano, 2012). A comparison of the corresponding micrographs in Figs. 8 and 9 also suggests that by increasing the culture period from 24 h to 48 h, an increase in the number of cells is observed. This confirms the cell proliferation realized in the MTT assay.

4. Conclusions

In this study, chitosan/fluoride-doped diopside coatings with the different amounts of the nanoparticles (20, 40, 60 and 80 wt%) were deposited on stainless steel 316 l by dip-coating. The immersion of the samples in the SBF for 14 days caused the precipitation of apatite layers around the reinforcing ceramic nanoparticles, showing the induced bioactive properties and apatite-formation ability. The corrosion results showed that the corrosion resistance of the coated samples was higher than that of the uncoated samples and was increased with increasing the nanoparticle content from 20% to 80%. The cytotoxicity results indicated that S-60% has the best behavior, while the cell adhesion on S-80% was optimal.

References

Abe, Y., Kokubo, T., & Yamamuro, T. (1990). Apatite coating on ceramics, metals and polymers utilizing a biological process. *Journal of Materials Science: Materials in Medicine, 1*(4), 233–238.

Baghjeghaz, M. J., & Salahinejad, E. (2017). Enhanced sinterability and in vitro bioactivity of diopside through fluoride doping. *Ceramics International, 43*(5), 4680–4686.

Bakhsheshi-Rad, H., Hamzah, E., Kasiri-Asgarani, M., Jabbarzare, S., Iqbal, N., & Kadir, M. A. (2016). Deposition of nanostructured fluorine-doped hydroxyapatite–polycaprolactone duplex coating to enhance the mechanical properties and corrosion resistance of Mg alloy for biomedical applications. *Materials Science and Engineering: C, 60*, 526–537.

Baskar, D., Balu, R., & Kumar, T. S. (2011). Mineralization of pristine chitosan film through biomimetic process. *International Journal of Biological Macromolecules, 49*(3), 385–389.

Bronzino, J. D., & Park, J. B. (2002). *Biomaterials: Principles and applications.* crc press.

Cai, Y., Zhang, S., Zeng, X., Wang, Y., Qian, M., & Weng, W. (2009). Improvement of bioactivity with magnesium and fluorine ions incorporated hydroxyapatite coatings via sol–gel deposition on Ti6Al4V alloys. *Thin Solid Films, 517*(17), 5347–5351.

Chandy, T., & Sharma, C. P. (1990). Chitosan-as a biomaterial. *Biomaterials, Artificial Cells and Artificial Organs, 18*(1), 1–24.

Di Martino, A., Sittinger, M., & Risbud, M. V. (2005). Chitosan: A versatile biopolymer for orthopaedic tissue-engineering. *Biomaterials, 26*(30), 5983–5990.

Diba, M., Goudouri, O.-M., Tapia, F., & Boccaccini, A. R. (2014). Magnesium-containing bioactive polycrystalline silicate-based ceramics and glass-ceramics for biomedical applications. *Current Opinion in Solid State and Materials Science, 18*(3), 147–167.

Diba, M., Tapia, F., Boccaccini, A. R., & Strobel, L. A. (2012). Magnesium-containing bioactive glasses for biomedical applications. *International Journal of Applied Glass Science, 3*(3), 221–253.

Ehsani, A., Moshrefi, R., & Ahmadi, M. (2015). Electrochemical investigation of inhibitory of New synthesized 3-(4-iodophenyl)-2-imino-2, 3-dihydrobenzo [d] oxazol-5-yl 4-methylbenzenesulfonate on corrosion of stainless steel in acidic medium. *Journal of Electrochemical Science and Technology, 6*(1), 7–15.

Esmati, N., Khodaei, T., Salahinejad, E., & Sharifi, E. (2018). Fluoride doping into SiO2-MgO-CaO bioactive glass nanoparticles: Bioactivity, biodegradation and biocompatibility assessments. *Ceramics International, 44*(14), 17506–17513.

Garcia, L. G. S., de Melo Guedes, G. M., da Silva, M. L. Q., Castelo-Branco, D. S. C. M., Sidrim, J. J. C., de Aguiar Cordeiro, R., ... Brilhante, R. S. N. (2018). Effect of the molecular weight of chitosan on its antifungal activity against candida spp. In planktonic cells and biofilm. *Carbohydrate Polymers*.

Groysman, A. (2009). *Corrosion for everybody*. Springer Science & Business Media.

Hahn, B.-D., Park, D.-S., Choi, J.-J., Ryu, J., Yoon, W.-H., Choi, J.-H., ... Kim, S.-G. (2011). Aerosol deposition of hydroxyapatite–chitosan composite coatings on biodegradable magnesium alloy. *Surface and Coatings Technology, 205*(8), 3112–3118.

Hosseini, Y., Emadi, R., Kharaziha, M., & Doostmohammadi, A. (2017). Reinforcement of electrospun poly (ε-caprolactone) scaffold using diopside nanopowder to promote biological and physical properties. *Journal of Applied Polymer Science, 134*(6).

Jouyban, A., Soltanpour, S., & Chan, H.-K. (2004). A simple relationship between dielectric constant of mixed solvents with solvent composition and temperature. *International Journal of Pharmaceutics, 269*(2), 353–360.

Jun, S.-H., Lee, E.-J., Yook, S.-W., Kim, H.-E., Kim, H.-W., & Koh, Y.-H. (2010). A bioactive coating of a silica xerogel/chitosan hybrid on titanium by a room temperature sol–gel process. *Acta Biomaterialia, 6*(1), 302–307.

Khor, E., & Lim, L. Y. (2003). Implantable applications of chitin and chitosan. *Biomaterials, 24*(13), 2339–2349.

Kim, H. W., Knowles, J. C., & Kim, H. E. (2005). Hydroxyapatite and gelatin composite foams processed via novel freeze-drying and crosslinking for use as temporary hard tissue scaffolds. *Journal of Biomedical Materials Research Part A, 72*(2), 136–145.

Kokubo, T., & Takadama, H. (2006). How useful is SBF in predicting in vivo bone bioactivity? *Biomaterials, 27*(15), 2907–2915.

Kong, L., Gao, Y., Lu, G., Gong, Y., Zhao, N., & Zhang, X. (2006). A study on the bioactivity of chitosan/nano-hydroxyapatite composite scaffolds for bone tissue engineering. *European Polymer Journal, 42*(12), 3171–3179.

Kumar, J. P., Lakshmi, L., Jyothsna, V., Balaji, D., Saravanan, S., Moorthi, A., ... Selvamurugan, N. (2014). Synthesis and characterization of diopside particles and their suitability along with chitosan matrix for bone tissue engineering in vitro and in vivo. *Journal of Biomedical Nanotechnology, 10*(6), 970–981.

Li, Z., Yubao, L., Aiping, Y., Xuelin, P., Xuejiang, W., & Xiang, Z. (2005). Preparation and in vitro investigation of chitosan/nano-hydroxyapatite composite used as bone substitute materials. *Journal of Materials Science: Materials in Medicine, 16*(3), 213–219.

Lim, J. Y., Taylor, A. F., Li, Z., Vogler, E. A., & Donahue, H. J. (2005). Integrin expression and osteopontin regulation in human fetal osteoblastic cells mediated by substratum surface characteristics. *Tissue Engineering, 11*(1-2), 19–29.

Lin, H. R., & Yeh, Y. J. (2004). Porous alginate/hydroxyapatite composite scaffolds for bone tissue engineering: Preparation, characterization, and in vitro studies. *Journal of Biomedical Materials Research Part B: Applied Biomaterials, 71*(1), 52–65.

Liu, X., Chen, S., Tian, F., Ma, H., Shen, L., & Zhai, H. (2007). Studies of protection of iron corrosion by rosin imidazoline self-assembled monolayers. *Surface and Interface Analysis, 39*(4), 317–323.

López-Pérez, P. M., da Silva, R. M., Serra, C., Pashkuleva, I., & Reis, R. L. (2010). Surface phosphorylation of chitosan significantly improves osteoblast cell viability, attachment and proliferation. *Journal of Materials Chemistry, 20*(3), 483–491.

Luz, G. M., & Mano, J. F. (2012). Chitosan/bioactive glass nanoparticles composites for biomedical applications. *Biomedical Materials, 7*(5), 054104.

Martens, C. S., & Harriss, R. C. (1970). Inhibition of apatite precipitation in the marine environment by magnesium ions. *Geochimica Et Cosmochimica Acta, 34*(5), 621–625.

Mota, J., Yu, N., Caridade, S. G., Luz, G. M., Gomes, M. E., Reis, R. L., ... Mano, J. F. (2012). Chitosan/bioactive glass nanoparticle composite membranes for periodontal regeneration. *Acta Biomaterialia, 8*(11), 4173–4180.

Peter, M., Binulal, N., Nair, S., Selvamurugan, N., Tamura, H., & Jayakumar, R. (2010). Novel biodegradable chitosan–gelatin/nano-bioactive glass ceramic composite scaffolds for alveolar bone tissue engineering. *Chemical Engineering Journal, 158*(2), 353–361.

Peter, M., Binulal, N., Soumya, S., Nair, S., Furuike, T., Tamura, H., ... Jayakumar, R. (2010). Nanocomposite scaffolds of bioactive glass ceramic nanoparticles disseminated chitosan matrix for tissue engineering applications. *Carbohydrate Polymers, 79*(2), 284–289.

Peter, M., Ganesh, N., Selvamurugan, N., Nair, S., Furuike, T., Tamura, H., ... Jayakumar, R. (2010). Preparation and characterization of chitosan–gelatin/nanohydroxyapatite composite scaffolds for tissue engineering applications. *Carbohydrate Polymers, 80*(3), 687–694.

Razavi, M., Fathi, M., Savabi, O., Razavi, S. M., Heidari, F., Manshaei, M., ... Tayebi, L. (2014). In vivo study of nanostructured diopside (CaMgSi 2 O 6) coating on magnesium alloy as biodegradable orthopedic implants. *Applied Surface Science, 313*, 60–66.

Rochet, N., Balaguer, T., Boukhechba, F., Laugier, J.-P., Quincey, D., Goncalves, S., ... Carle, G. F. (2009). Differentiation and activity of human preosteoclasts on chitosan enriched calcium phosphate cement. *Biomaterials, 30*(26), 4260–4267.

Salahinejad, E., & Baghjeghaz, M. J. (2017). Structure, biomineralization and biodegradation of Ca-Mg oxyfluorosilicates synthesized by inorganic salt coprecipitation. *Ceramics International, 43*(13), 10299–10306.

Salahinejad, E., & Vahedifard, R. (2017). Deposition of nanodiopside coatings on metallic biomaterials to stimulate apatite-forming ability. *Materials & Design, 123*, 120–127.

Salahinejad, E., Hadianfard, M., Macdonald, D., Mozafari, M., Walker, K., Rad, A. T., ... Tayebi, L. (2013). Surface modification of stainless steel orthopedic implants by sol–gel ZrTiO4 and ZrTiO4–PMMA coatings. *Journal of Biomedical Nanotechnology, 9*(8), 1327–1335.

Serre, C., Papillard, M., Chavassieux, P., Voegel, J., & Boivin, G. (1998). Influence of magnesium substitution on a collagen–apatite biomaterial on the production of a calcifying matrix by human osteoblasts. *Journal of Biomedical Materials Research Part A, 42*(4), 626–633.

Sharifi, E., Azami, M., Kajbafzadeh, A.-M., Moztarzadeh, F., Faridi-Majidi, R., Shamousi, A., ... Ai, J. (2016). Preparation of a biomimetic composite scaffold from gelatin/collagen and bioactive glass fibers for bone tissue engineering. *Materials Science and Engineering: C, 59*, 533–541.

Sharifi, E., Ebrahimi-Barough, S., Panahi, M., Azami, M., Ai, A., Barabadi, Z., ... Ai, J. (2016). In vitro evaluation of human endometrial stem cell-derived osteoblast-like cells' behavior on gelatin/collagen/bioglass nanofibers' scaffolds. *Journal of Biomedical Materials Research Part A, 104*(9), 2210–2219.

Singh, T. P., Singh, H., & Singh, H. (2012). Characterization, corrosion resistance, and cell response of high-velocity flame-sprayed HA and HA/TiO2 coatings on 316L SS. *Journal of Thermal Spray Technology, 21*(5), 917–927.

Tanahashi, M., & Matsuda, T. (1997). Surface functional group dependence on apatite formation on self-assembled monolayers in a simulated body fluid. *Journal of Biomedical Materials Research: An Official Journal of The Society for Biomaterials and The Japanese Society for Biomaterials, 34*(3), 305–315.

Tanahashi, M., Yao, T., Kokubo, T., Minoda, M., Miyamoto, T., Nakamura, T., ... Yamamuro, T. (1994). Apatite coating on organic polymers by a biomimetic process. *Journal of the American Ceramic Society, 77*(11), 2805–2808.

Teng, S. H., Lee, E. J., Yoon, B. H., Shin, D. S., Kim, H. E., & Oh, J. S. (2009). Chitosan/nanohydroxyapatite composite membranes via dynamic filtration for guided bone regeneration. *Journal of Biomedical Materials Research Part A, 88*(3), 569–580.

Thein-Han, W., & Misra, R. (2009). Biomimetic chitosan–nanohydroxyapatite composite scaffolds for bone tissue engineering. *Acta Biomaterialia, 5*(4), 1182–1197.

Vahedifard, R., & Salahinejad, E. (2017). Microscopic and spectroscopic evidences for multiple ion-exchange reactions controlling biomineralization of CaO. MgO. 2SiO2 nanoceramics. *Ceramics International, 43*(11), 8502–8508.

Wang, J., de Boer, J., & De Groot, K. (2004). Preparation and characterization of electrodeposited calcium phosphate/chitosan coating on Ti6Al4V plates. *Journal of Dental Research, 83*(4), 296–301.

Wang, X., Wang, X., Tan, Y., Zhang, B., Gu, Z., & Li, X. (2009). Synthesis and evaluation of collagen–chitosan–hydroxyapatite nanocomposites for bone grafting. *Journal of Biomedical Materials Research Part A, 89*(4), 1079–1087.

Wu, C., & Chang, J. (2007). Degradation, bioactivity, and cytocompatibility of diopside, akermanite, and bredigite ceramics. *Journal of Biomedical Materials Research Part B: Applied Biomaterials, 83*(1), 153–160.

Yadav, M., Kumar, S., Kumari, N., Bahadur, I., & Ebenso, E. E. (2015). Experimental and theoretical studies on corrosion inhibition effect of synthesized benzothiazole derivatives on mild steel in 15% HCl solution. *International Journal of Electrochemical Science, 10*, 602–624.

Yu, H., Wooley, P. H., & Yang, S.-Y. (2009). Biocompatibility of poly-ε-caprolactone-hydroxyapatite composite on mouse bone marrow-derived osteoblasts and endothelial cells. *Journal of Orthopaedic Surgery and Research, 4*(1), 5.